Design, Modeling and Control of Soft Syringes Enabling Two Pumping Modes for Pneumatic Robot Applications

Jianshu Zhou, *Member*, *IEEE*, Junda Huang, Xin Ma, Andy Lee, Kazuhiro Kosuge, *Fellow, IEEE*,
and Yunhui Liu, *Fellow, IEEE*.

Abstract — Pneumatic actuation is important in robotic applications, such as manipulating objects in interaction scenarios using pneumatic grippers and suction cups. However, traditional pneumatic actuation approaches, including industrial pneumatic systems and syringe pumps, suffer from limitations such as bulky systems, noisy operation, and inflexible pressure modulation, which limit their practicality for daily use. To address these challenges, we proposed a novel soft syringe and its corresponding Soft-Syringe (SS) pump. Moreover, we developed a two-mode pumping mechanism (direct and continuous pumping) for both positive and negative pressure outputs, enabling flexible pressure modulation. A detailed description of the soft syringe's design, modeling, control, and performance is provided. Additionally, a keyframe model is introduced to simplify the modeling of pressure dynamic response. The soft syringe showcases the benefits of low friction, high operational frequency (6.5 Hz), low noise (55.6 dB), and sufficient pressure range (-0.08MPa to 0.15MPa). Experimental results demonstrate the promise of the proposed approach for diverse pneumatic end-effector actuation and control with excellent modulation and scalability in human-centered scenarios.

Keywords: Soft Actuation, Soft pump, Syringe pump, Direct pumping, Continuous Pumping, Soft Robot Application.

I. Introduction

With the growing trend of robots moving out of factories and into everyday life, there is an increasing demand for robots to be designed and optimized for human-centered tasks [1], [2]. In particular, robotic grasping and manipulation are important functions for robots to interact with the real world [3], [4]. In traditional factory scenarios, robots are often used to handle large and heavy objects in structured environments, such as palletizing, de-palletizing, and large-load picking. To accomplish these tasks, the end-effector actuation has been predominantly based on industrial pneumatic actuation, which relies on an industrial gas source, air compressor, solenoid valves, and vacuum generator to provide large pressure extremes and flow rates [5]–[7]. Unlike industrial applications, human-centered tasks require higher safety standards, and are often carried out in unstructured environments. These tasks generally include grasping and manipulating everyday objects within the human hand's manageable size and weight, typical in robotic picking stations, cooking automation, rehabilitation, and service robotics. Consequently, in such human-centric applications, the desired features for pneumatic pumps include low noise, compact size, lightweight, rapid deployment, and versatile actuation modes [8]–[11].

However, achieving pneumatic actuation in human-centered applications remains a multifaceted challenge, encompassing all the previously mentioned factors. To address these challenges and pneumatically drive those robots, a prevalent approach involves utilizing a large air pump or industrial air sources in conjunction with a series of pneumatic accessories. This setup uses vacuum generators or pumps and auxiliary valves for flexible switching between positive and negative pressure. Despite efforts to enhance compactness by replacing critical components with smaller counterparts, such as portable electric pumps, significant challenges persist [9], [10].

Inspired by natural pumping mechanisms, some research has introduced innovative actuation techniques. They eliminate the need for electric pumps, with a particular emphasis on utilizing soft materials. One representative method is the self-pumping strategy using a fiber-reinforced silicone soft actuator combined with tendon-driven movement, which allows for untethered pneumatic action without relying on an electronic pump [12]. The other notable technique is the soft pump driven by the migration of electrons and ions, demonstrating applications in fully soft-bodied devices with outstanding portability [13]. Additionally, researchers have explored the use of dielectric elastomers with high energy density, fast response, and lightweight for several artificial pumping applications, such as magnetically coupled DE pumps [14], soft DE peristaltic pumps [15], and dielectric-fluid-amplified pumps [16], among others. While these novel pumps address certain challenges, their performance remains inferior to existing electronic pump-enabled pneumatic actuation, as they exhibit limitations in actuation efficiency, pressure adjustment accuracy, actuation flexibility, pressure range, and durability [9], [10].

Syringe pumps are widely used in pneumatic robots and soft robots due to their flexibility and stability on the pressure tuning and low noise properties. However, their rigid structure and reliance on piston-based actuation limit their broader application in robotics, particularly in scenarios with high-frequency demands and spatial constraints. Using a soft

This work is supported by the Shenzhen Portion of Shenzhen-Hong Kong Science and Technology Innovation Cooperation Zone under HZOB KCZYB 20200089, in part by the CUHK T Sone Robotics Institute, in part by the InnoHK of the Government of the Hong Kong Special Administrative Region via the Hong Kong Centre for Logistics Robotics, and the Research Grants Council of Hong Kong (GRF No. 14207320, and 14207423).Corresponding: Yunhui Lin; Xin Ma (yhliu@cuhk.edu.hk; xinma001@cuhk.edu.hk)

JS. Zhou, JD. Huang, X. Ma, Andy, and YH. Liu are with Department of Mechanical and Automation Engineering, The Chinese University of Hong Kong.

K. Kosuge is with the Department of Electrical and Electronic Engineering. The University of Hong Kong.

JS. Zhou and YH. Liu are also with the Hong Kong Center for Logistics Robotics.

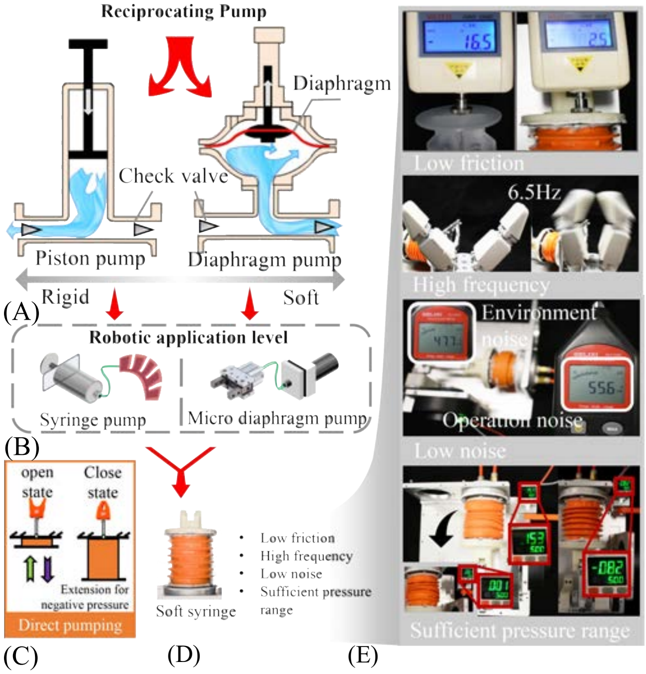

Figure 1. Concept of the soft syringe. (A) Structure and classification of reciprocating pump. (B) Reciprocating pump used at the robotic application level. (C) Mechanism of the direct pumping of the syringe pump. (D) Soft syringe and its merits. (E) Experiments on average friction, operation frequency, noise comparation, and functional pressure range.

actuator as a pumping chamber to create pressure changes has been identified as a promising direction for artificial pumping [17], [18]. Some related works have investigated the use of soft bellows as the main body of reciprocating pneumatic pumps, for example the soft bellows pumps proposed by [19]–[21]. They utilize tendon-driven approaches to drive an end-effector directly, however, the concept of soft syringes has not yet been sufficiently emphasized, with several challenges still to be addressed in these soft pumping solutions. Firstly, common soft actuators often lack sufficient stiffness for large-pressure pumping, as their elastic chambers tend to buckle under high pressure or vacuum conditions. As a result, not only is the output pressure range restricted, but achieving negative pressure also becomes challenging. Secondly, controlling and repeating the deformation of a soft actuator is difficult [16], leading to pressure instability and decreased durability. Lastly, the bandwidth is limited. Similar to the syringe pump, which dissipates a large portion of work through its piston, the energy dissipation of soft bellows mainly comes from the elasticity of soft material.

In this paper, we leverage emerging soft robotics technology to address challenges of traditional rigid syringe pumps while maintaining soft robotics' advantages of low noise and flexible pressure modulation. We proposed a novel soft syringe capable of withstanding positive and negative pressures without buckling, while ensuring repeatable volume deformation [22]. Additionally, we introduce a two-mode pumping mechanism using check valves and four controllable solenoid valves. This design enables switching between continuous pumping and direct pumping modes. Continuous pumping enables a continuous airflow at the outlet, typically requiring two or more soft syringes, with air exchange with the atmosphere. In contrast, direct pumping is an intuitive pumping mode connecting the syringe with the actuation target without air exchange with the atmosphere. Furthermore, we develop a model-based closed-loop pressure controller that reduces pressure fluctuations during dynamic and steady-state stages. Performance evaluations demonstrate the soft syringe's merits of low noise, low damping, high-frequency operation, a flexible pressure modulation range, and repeatability. To illustrate the versatility and potential applications of our approach, we have employed a pair of soft syringe in an SS pump across four typical robotic applications, i.e., continuous positive and negative pressure actuation, high-frequency pneumatic switching, and flexible pressure modulation.

Highlights of the contributions:

- The concept of the soft syringe is introduced, and a novel soft-syringe (SS) actuator, reinforced by rigid ribs, is proposed. The SS pump, utilizing the SS-actuator, is capable of achieving low noise, low friction, high-frequency motion, and flexible pressure modulation, making it suitable for various robotics applications.
- A novel two-mode pumping mechanism is developed, allowing for switching between continuous pumping and direct pumping.
- The nonlinear pressure model of SS-actuators is separated into three simplified models for real-time pressure control, including the simplified flow rate model, pressure extremum model, and key-frame-based pressure dynamic response model, where the keyframe model of SS-actuators is first proposed.

In the following sections, the concept, design, fabrication, and modeling of soft syringes and two-mode pumping are discussed with experimental validation.

II. Two-mode Pumping Enabled by Soft Syringe

In this section, we first introduce the concept of the soft syringe and compare the SS pump with other pumps. Next, we present the design and fabrication of the soft syringe. Finally, we demonstrate the two-mode pumping mechanism achieved through the soft syringe.

A. Concept of Soft Syringe

In human-centered robotic applications, pneumatic end-effectors such as pneumatic grippers, suction cups, and pneumatic actuators demand a compact and portable air source with low operating noise, flexible pressure modulation, and the ability to generate both positive and negative pressures [23]–[27]. The syringe pump directly connects its chamber to the pneumatic actuator, enabling flexible pressure modulation and maintenance [28], [29]. Its structure consists of a rigid cylinder and a rubber piston with an interference fit to ensure air tightness. Since the syringe pump controls airflow by reciprocating the piston, it is classified as a reciprocating pump (Fig. 1A). However, due

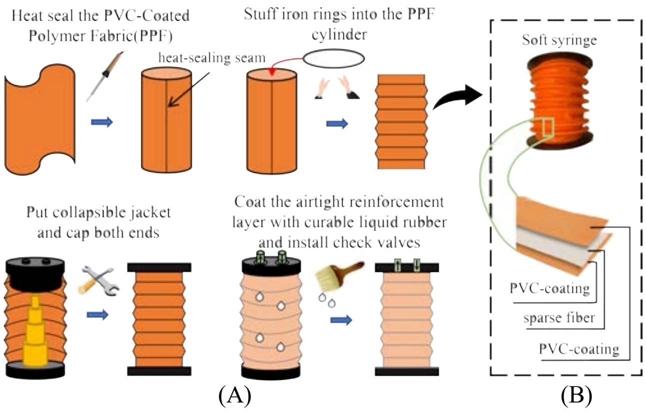

Figure 2. Fabrication of soft syringe. (A) Fabrication process of soft syringe. (B) Structure of the PPF.

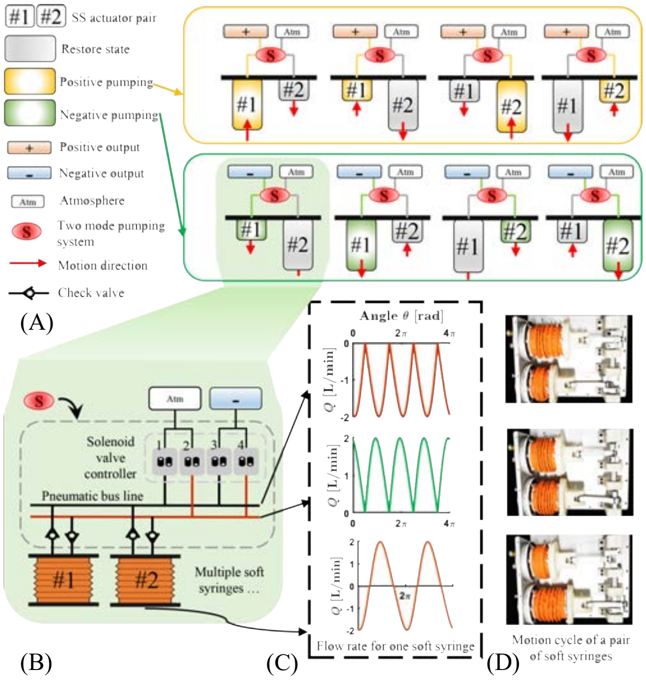

Figure 3. Two pumping modes, direct and continuous pumping mechanism. (A) Continuous pumping with positive pressure and negative pressure. (B) Structure of two mode pumping system. (C) Flow rate of the two air bus line and soft syringe under constant operation speed. (D) A half motion cycle of a pair of SS-actuators.

to the piston serving as an airtight component, its friction increases with larger syringe volumes and higher pressures, making it challenging to achieve high-frequency reciprocating motion.

On the other hand, because the syringe pump system is isolated from the atmosphere, any air leakage in the channels can cause performance and calibration issues. We term this pumping method as direct pumping (Fig. 1C), and a similar concept in [21] is referred to as "self-pumping." In contrast, continuous pumping is a method where the airflow at the outlet continuously flows in one direction, allowing for continuous air replenishment (Fig. 3A). By controlling the airflow direction, we can achieve continuous positive and negative pressure modulation.

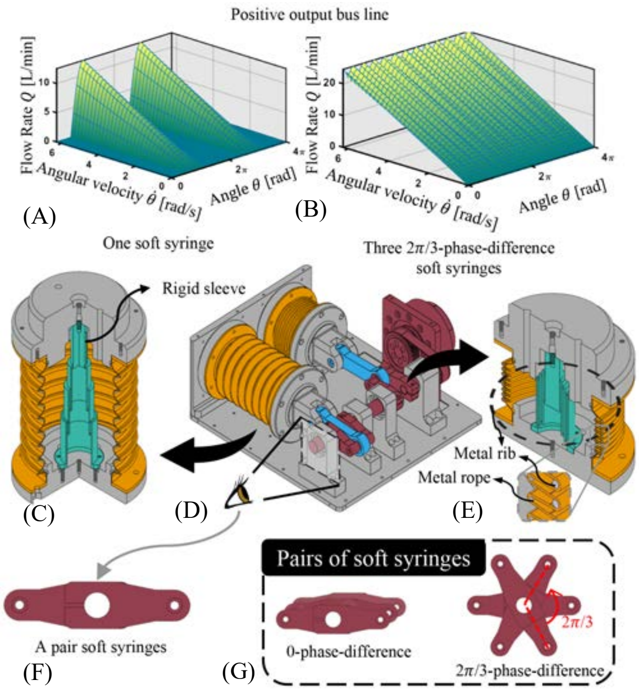

Figure 4. Design of the SS-actuator and SS pump. (A) and (B) are the positive flow rate model of one SS-actuator and three SS-actuators. (C) Cross-section view of the extended SS-actuator. (D) Structure of the SS pump. (E) Cross-section side view of the compressed SS-actuator. (F) Side view of a pair of SS-actuators. (G) Two phase states of three pairs of SS-actuators.

Another variety of reciprocating pump is the diaphragm pump, characterized by its utilization of a soft structure within the pumping mechanism. This type of pump creates pressure by pushing a flexible diaphragm with a piston, a process coordinated with check valves to maintain a continuous flow (as depicted in Fig. 1A).

In contrast to a syringe pump, the piston in a diaphragm pump offers linear motion instead of ensuring airtightness, which results in reduced friction. However, it's essential to note that due to the unpredictable and limited deformations of the soft diaphragm, diaphragm pumps are best suited for continuous pumping applications.

The introduction of the soft syringe represents a novel attempt to replace traditional rigid components with soft and deformable components in reciprocating pumps. The soft syringe and its induced SS pump integrate the advantages of the syringe pump and the diaphragm pump (Fig. 1B), with low noise, flexible pressure modulation, a wide pressure range, high frequency, and the ability to realize two pumping modes.

B. Design and Fabrication of Soft Syringe

The SS-actuator consists of a soft syringe with origami features and a rigid sleeve for motion guidance (Fig. 4C and 4E). The dimensions of the SS-actuator can be highly customized depending on the application scenario. The key parameters, including *d*, *D*, *n*, and *H*, define the depth and number of zig-zag features (Fig. 6A), thus influencing core properties such as the extension ratio, elastic force, and buckling behavior. To improve the zig-zag feature's strength and enable higher pressure and buckling resistance, metal ribs are introduced. This research focuses on the SS-actuator's use in robotic end-effector actuation, encompassing tasks like robotic grippers and suction cups. The dimensions of the SS-actuator are carefully selected to align with a previous soft gripper design [18], [25], [30], [31] developed by the authors, which is tailored for grasping everyday objects, and the chosen design parameters for this prototype SS-actuator are illustrated in Table I.

TABLE. I. MAJOR PARAMETERS OF THE SS-ACTUATORS

Parameters	Values
Small diameter: d (mm)	50
Large diameter: D (mm)	55
Chamber wall thickness (mm)	0.6
Residual volume: V_{res} (mL)	69
Minimum length (mm)	45
SS-actuator stroke (mm)	30
Original length: H_0 (mm)	75
Weight (g)	60
Number of folds: n	7
Linkage 1: L (mm)	58
Linkage 2: r (mm)	15

Figure 2A displays the fabrication process of the soft syringe, crafted from a lightweight, resilient, foldable, and airtight PVC-coated polymer fabric (EITEC, Taicang), as detailed in Figure 2B. The process starts by bending this fabric, with its dual layers of PVC-coated sparse polymer fibers, into a cylinder and heat-sealing the seams. Metal ribs are then inserted into specifically designed 'mountain' positions to form a zig-zag pattern, as referenced in [25][26] , with the fabric's strength and resilience preventing tearing at the joints. Metal ropes wrapped around each 'valley' augment pressure resistance. Following this, a sealing cap and a linear piston guide, which reduces friction by acting solely as a guide rather than resisting pressure like in traditional syringe pumps, are added. Optionally, the syringe's outer layer can be silicone-coated for enhanced air tightness and a broader pressure range.

C. Two-mode Pumping using Soft Syringe

The two-mode pumping includes continuous pumping and direct pumping, as discussed in the previous section. Continuous pumping enables a continuous airflow at the outlet port, allowing pressurization of objects larger than the pump itself and compensating for air leakage in pneumatic actuation (Fig. 3A). On the other hand, direct pumping offers flexible pressure modulation between positive and negative values, ensuring stable pressure maintenance (Fig. 1C). The two-mode pumping system is achieved using four solenoid valves and multiple check valves, as illustrated in Figure 3B. Each SS-actuator is connected to two check valves and then mounted to two bus lines, similar to parallel equipment. Then the two bus lines are separately connected to two solenoid valves, one linked to the atmosphere and the other to the pneumatic equipment (Fig. 3B).

To achieve direct pumping, solenoid valves 1 and 2 are kept closed, while valves 3 and 4 are opened, as depicted in Figure 5. For continuous pumping, the state of the solenoid valves dynamically switches, as detailed in the pressure control section. Notably, while the state is dynamically changing, valve pairs (2,3) and (1,4) are coupled to simultaneously open or close, while pair (1,3) and pair (2,4) exhibit opposite states (Fig. 5).

Continuous pumping

Sole Valve	1	2
3	~	&
4	&	~

Direct pumping

1	close	3	open
2	close	4	open

opposite open/close state: ~
same open/close state: &

Figure 5. The open and close state of solenoid valves.

In this work, we implement two-mode pumping in the SS pump, which is based on one or multiple soft syringes. The SS pump with a pair SS-actuator is presented in Figure 4D. In continuous pumping, the motor rotates in one direction, driving the reciprocating motion of the soft syringe. However, due to the check valves, the airflow on each air bus line changes periodically under the pressure constraint, as illustrated in Figures 3C. On the other hand, in direct pumping, two bus lines are interconnected, causing the SS pump to behave like a syringe pump. For the SS pump with multiple SS-actuators, the phase difference introduces more complex airflow. In our investigation, we focus on SS-actuator pairs with a phase difference of π, as shown in Figure 4F. The simplified side view of the SS pump in Fig. 4G shows the phase differences of the SS-actuators, where 0-phase-difference indicates that each of the three pairs of SS-actuators has no phase difference, and 2π/3-phase-difference indicates that each pair has a phase difference of 2π/3. It is worth mentioning that in continuous pumping, our SS pump can achieve flexible positive and negative pressure modulation, which is crucial for robotic end-effector applications, thanks to the high-frequency motion capability of the soft syringe.

III. Soft Syringe and Pumping System Modeling

The pumping system (Figs. 3C and 3D), due to soft deformation, pressure balance, and valves, introduces nonlinearity to the relationship between motor speed and the target container's pressure [16]. Unlike the nonlinearity introduced by the pressure of the SS-actuator and deformation [27][28], discontinuity introduced by the valves makes it challenging to develop an accurate model for pressure control using the ideal gas law, especially in the case of using multiple pairs of SS-actuators for pumping [29][30].

To overcome this challenge, we simplify the complex nonlinear model into three separate models, i.e., the flow rate model, the keyframe dynamic response model for pressure (A keyframe application could be refered to [38]), and the pressure extremum model. For example, in the simplified flow rate model, we assume that the atmosphere port and negative port of the two-mode pumping system have the same pressure and an infinite volume (Fig. 3B). Therefore, in this section, we investigate these three models considering multiple SS-actuators, check valves, and four solenoid valves for pressure control of continuous pumping. As direct pumping manipulates a fixed air quantity, these models focus on the behavior of continuous pumping.

A. Flow Rate Model

The flow rate model aims to establish the relationship between the motor speed and the flow rate at the negative output port, as shown in Fig. 3B. This simplified flow rate model assumes that the atmosphere port and negative port of the two-mode pumping system have identical pressure and an infinite volume, which we call it as identical-pressure assumption in the subsequent context. Therefore, the performance of this linearized model gradually becomes less accurate when the pressure difference between these two ports increases. The reason is that the flow rate model becomes increasingly nonlinear as the pressure difference increases. This nonlinearity is further analyzed in the pressure dynamic response model and experiment section.

The flow rate model is formulated in two steps for multiple SS-actuators with different phases. First, a flow rate model of a SS-actuator without valves is attained. In the next step, the check valves and solenoid valves are considered in the model.

Given the rotational symmetry of the SS-actuator around its central axis, the volume of the i-th SS-actuator, which can be viewed as a series of stacked cones, is

$$\begin{aligned} V_i &= \frac{\pi(D^2+Dd+d^2)}{12}\cdot(H_0+q_0-q_i) \\ &= a\cdot(H_0+q_0-q_i), \qquad i=1,\dots n \end{aligned} \tag{1}$$

where D is the diameter of the mountain fold, d is the diameter of the valley fold, q_i is the distance from the rotation axis to the SS-actuator's surface of the i-th SS-actuator, H_0 and q_0 represent the original length of the SS-actuator and q_i when linkage position is at the 0 °, respectively. The SS-actuator's configurations and parameters can be seen from the Fig. 6A, and we substitute $\frac{\pi(D^2+Dd+d^2)}{12}$ with a for simplification.

Then, q_i can be attained by applying the law of cosines,

$$q_i^2 + r^2 - 2q_i r\cdot\cos\left(\frac{\pi}{2}-\theta-\theta_i\right) = L^2 \tag{2}$$

where r and L is the length of the rotation linkage and the SS-actuator linkage, θ is the motor's rotation angle, θ_i is the phase of the i-th SS-actuator. As the motor only rotates in one direction, the solution to the Eq. 2 is $q_i = r\cdot\sin(\theta+\theta_i) + \sqrt{L^2 - r^2\cdot\cos^2(\theta+\theta_i)}$ by choosing the positive direction as the rotation direction.

We derive the SS-actuator flow rate model without considering valves in this first step by computing the derivative of the SS-actuator's volume. It is worth mentioning that the derivation separates θ and $\dot{\theta}$, which enables us to forwardly compute the motor speed from the desired flow rate.

$$\dot{V}_i = -a\cdot\dot{q}_i = -a\cdot\frac{dq_i}{d\theta}\frac{d\theta}{dt} \tag{3}$$

Based on Eq. 3, we obtain the flow rate Q_i at the negative output port by integrating check valves and solenoid valves into V_i (Fig. 3B), which is expressed as a piecewise function considering the opening and closing of the valves,

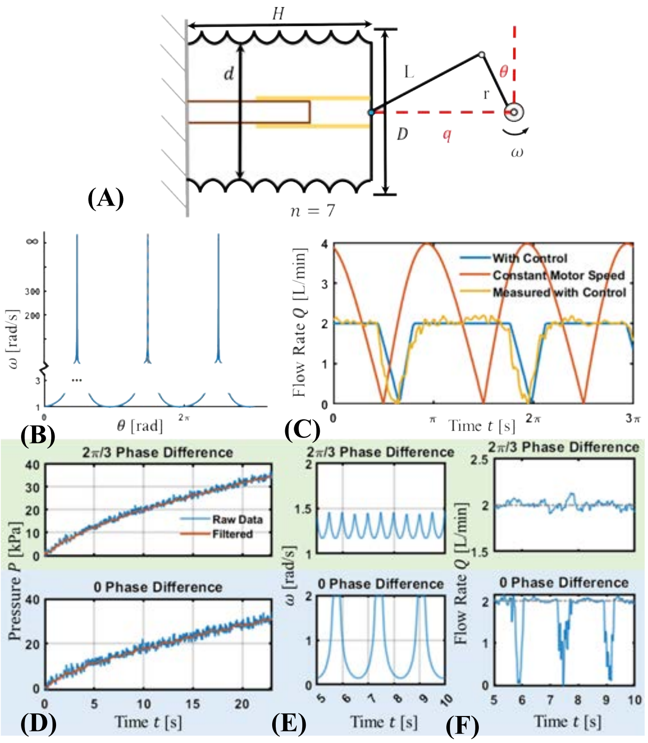

Figure 6. (A) SS-actuator model. (B) is the desired angular velocity to maintain a constant flow rate for a pair of SS-actuator. (C) shows the comparison between controlled and uncontrolled flow rate for a pair of SS-actuators. Measured flow rate with flow rate control is shown with the yellow line. (D), (E), and (F) are measured pressure, desired angular velocity, and flow rate attained from differentiated pressure of three pairs of SS-actuators. Green part has setup as $2\pi/3$-phase-difference, and blue part is 0-phase-difference.

$$Q_i = \begin{cases} -\dot{V}_i & -\operatorname{sgn}(Q_r)\cdot\dot{V}_i > 0 \\ 0 & -\operatorname{sgn}(Q_r)\cdot\dot{V}_i \le 0 \end{cases} \tag{4}$$

where Q_i is the flow rate of the i-th SS-actuator at the negative output port, Q_r is the desired flow rate, which is also the reference flow rate of the controller (Fig. 8B). When the referenced flow rate Q_r has the same direction with the SS-actuator's flow rate $-\dot{V}_i$, $Q_i = -\dot{V}_i$, otherwise, $Q_i = 0$, as the airflow is directed to the atmosphere (atom port) as shown in Figure 3B. This can be further simplified to the Eq. 5 as SS-actuator:

$$Q_i = \frac{1}{2}\dot{V}_i\left(\operatorname{sgn}(Q_r)\operatorname{sgn}(\dot{V}_i) - 1\right) \tag{5}$$

We obtain the flow rate of a multiple SS-actuators system by summarizing all SS-actuators flow rate Q_i up,

$$Q = \sum_i Q_i = \sum_i f(\theta+\theta_i)\cdot\dot{\theta} \tag{6}$$

where Q is the total flow rate of the SS pump. Figure 4A presents the flow rate of a single SS-actuator, while Figure 4B demonstrates the flow rate of three SS-actuators with a $2\pi/3$-phase-difference.

Figure 6 (B-F) shows two examples of flow rates: one with a pair of SS-actuators and another with three pairs. Each pair has two SS-actuators with a phase difference of π, as seen in Fig. 4F. For a pair of SS-actuators, there exists a singularity point on ω for a desired constant flow rate (Fig. 6B), which necessitates the definition of a maximum angular velocity in the experiment, for example, without loss of generality, the maximum angular velocity is set as $2\ rad/s$ in Fig. 6E. As shown in Figure 6C, when the desired flow rate $Q_r = 2$, due to the singularity, the theoretical flow rate is shown in the blue line, while the measured flow rate using the open loop controller is shown in the yellow line. The orange line represents the flow rate under a constant ω, whose integral area should equal the integral area of the blue line.

Based on the flow rate Q, we can also evaluate the average flow rate $\bar{Q}$ as follow:

$$\bar{Q} = \frac{1}{T}\sum_{i}\int_{0}^{2\pi} f(\theta + \theta_i)\, d\theta \tag{7}$$

where $\bar{Q}$ is the average flow rate, $T = \frac{2\pi}{\omega}$, is the cycle of function f according to t.

B. Pressure Extremum

In the previous section, it was assumed that the inlet and outlet ports of the SS pump were connected to the atmosphere to obtain the flow rate model. However, in real scenarios, one of the ports (for example the negative output port in Figure 3B) is connected to the container while the other port is connected to the atmosphere. This results in the discontinuity of the flow rate, for example, if the pressure in the container is higher than the atmosphere while the other port is connected to the atmosphere, the check valve to the container will not open until the SS-actuator is compressed to the same pressure as the container.

Therefore, the pressure of the SS-actuators has upper and lower limits. To reach the upper limit, the control law of the continuous pumping for the solenoid valves should be implemented in the corresponding SS pump controller, which also satisfies the valve states in Fig. 5, and will be discussed in the control section. When the pressure in the container equals the pressure the SS-actuators can reach at q_{max}, based on the ideal gas law $PV = constant$, the upper pressure extremum can be attained as

$$P_{max} = P_a \cdot \frac{V_{res} + \Delta V}{V_{res}} \tag{8}$$

where P_a is the pressure of the atmosphere, ΔV is the changeable volume of the SS-actuator, V_{res} is the residual volume when the SS-actuator is compressed to its smallest volume (Fig. 4E). On the contrary, by opening the inlet solenoid valve to the container and outlet solenoid valve to the atmosphere, we achieve the lower pressure extremum

$$P_{min} = P_a \cdot \frac{V_{res}}{V_{res} + \Delta V} \tag{9}$$

where P_{max} and P_{min} are the extreme pressure that one SS-actuator can generate. It is worth mentioning that this pressure extremum still holds for multiple SS-actuators.

C. Keyframe of Pressure Dynamic Response Model

In this section, we investigate the nonlinearity property of the pressure dynamic response of the SS pump. The continuous dynamic response of the pressure is a highly nonlinear function that is affected by various time-variant variables, including the motor speed, the pressure difference between the inlet and outlet ports, the state of the solenoid valves, and the pressure of the SS-actuators.

Despite the complex nature of the dynamic response, our objective is not to obtain the continuous dynamic response of the pressure but rather to identify those key pressure points [38], which we refer to as pressure keyframes, in the process of the dynamic response. For pressures greater than 0, the keyframe pressure corresponds to the pressure at the position of the smallest volume, as shown in Figure 4E. Conversely, for pressures less than 0, the keyframe pressure is identified at the position of the largest volume, as shown in Figure 4C.

For the positive desired pressure, $P_r > 0$, the pressure of $(k-1)$-th cycle and k-th have the equilibrium

$$P_{k-1} \cdot V + P_a \cdot (V_{res} + \Delta V) = P_k \cdot (V_{res} + V) \tag{10}$$

where P_{k-1} is the $(k-1)$-th pressure keyframe, P_k is the k-th pressure keyframe, V is the volume of the container, ΔV is the changeable volume of the SS-actuator, P_a is the pressure of the atmosphere. The solution P_n of Eq. 10 is attained as $\left(P_a \cdot \frac{V_{res}+\Delta V}{V_{res}} - P_0\right)[1 - \left(\frac{V}{V+V_{res}}\right)^n]$, where P_0 is the initial pressure keyframe.

For the negative desired pressure, $P_r < 0$, we use the same method to analyze the discrete dynamic response

$$P_a \cdot V_{res} + P_{k-1} \cdot V = P_k \cdot (V_{res} + \Delta V + V) \tag{11}$$

where the solution of this negative response P_n is, $\left(P_a \cdot \frac{V_{res}}{V_{res}+\Delta V} - P_0\right)[1 - \left(\frac{V}{V+V_{res}+\Delta V}\right)^n]$.

IV. Pressure Control of Continuous Pumping

We present two closed-loop controllers for pressure control, where one is a model-free PID controller, the other is a model-based flow rate controller, as shown in the Fig. 8. Both controllers use the control output u for the solenoid valves control and motor speed control.

Model-free PID controller. Given the current pressure error, $e = P_r - P_t$, and normal PID control output, u, the motor speed is controlled by $\omega = |u|$ and solenoid valves are controlled by $sgn(u)$ signal. When $sgn(u)$ equals 1, solenoid valves 2, 3 are opened and 1, 4 are closed (Fig. 3B and Fig. 5), allowing for positive flow rate, and increasing the pressure. On the other hand, when $sgn(u)$ equals -1, solenoid valves 2, 3 are closed and 1, 4 are opened, resulting in a negative flow rate, and decreasing the pressure.

Model-based flow rate controller. The model-based controller is composed of two independent parts, which are a PID regulator and a forward model-based solver, as shown in the Figure 8B. The PID regulator generates a desired flow rate, Q_r , based on the current pressure P and desired pressure P_r, which is the same as the model-free controller. This desired flow rate is then sent to the solver, which computes the desired motor speed and solenoid valves' states using the flow rate model. Solenoid valves are controlled by $sgn(Q_r)$ signal. When $sgn(Q_r) = 1$, solenoid valves 2, 3

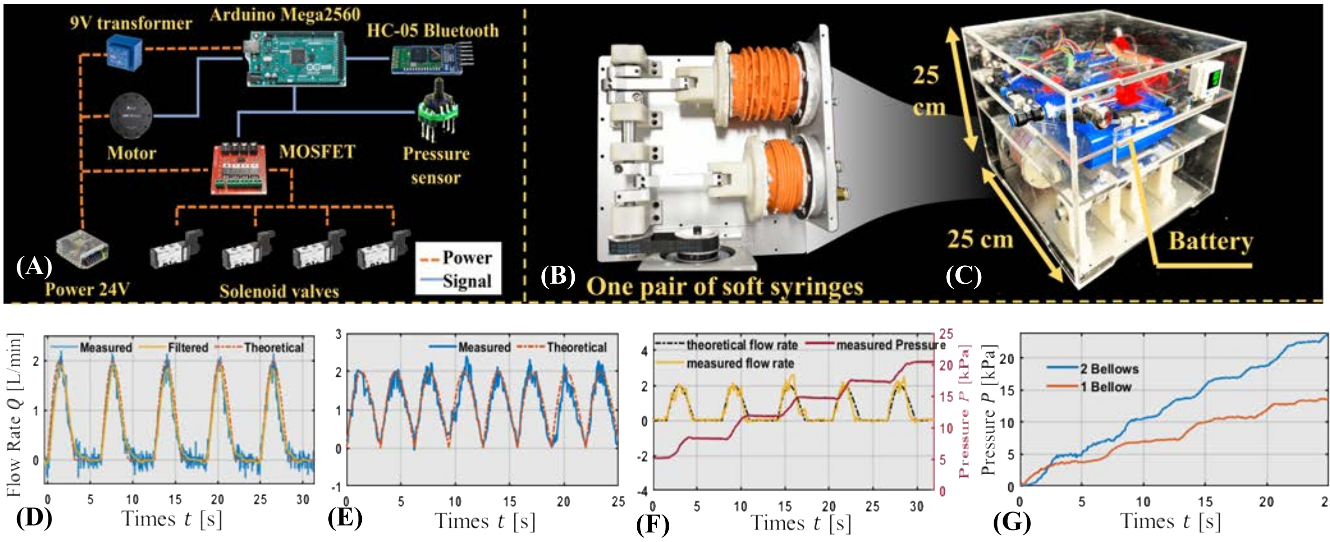

Figure 7. Experiment setup. (A) Electrical components diagram. (B) The mechanical structure of SS pump with a pair of SS-actuators used in the applications. The SS pump with three pairs of SS-actuators is extended based on this same configuration. (C) The experimental setup of SS pump with a pair of SS-actuators. (D) and (E) present the validation of flow rate model of one SS-actuator and a pair of SS-actuators, respectively. (F) Estimated flow rate based on measured pressure. One SS-actuator is employed. (G) Pressure comparation between one SS-actuator and a pair of SS-actuators, which are driven under the same angular velocity.

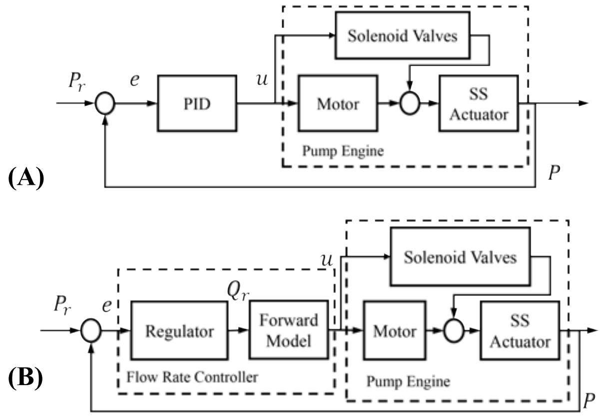

Figure 8. Control diagrams. (A) Model-free pressure control based on PID. (B) Model-based pressure control based on flow rate model.

are opened and 1, 4 are closed (Fig. 3B and Fig. 5), allowing for positive flow rate, and increasing the pressure. On the other hand, when $sgn(Q_r) = -1$, solenoid valves 2, 3 are closed and 1, 4 are opened, resulting in a negative flow rate, and decreasing the pressure. The motor speed is attained based on Eq. 6, where the motor speed $\omega = \dot{\theta}$ can be computed based on the current motor angle θ and flow rate $Q = Q_r$. The motor speed command is then sent to the motor to achieve the desired flow rate. By using the flow rate model, the change in pressure is expected to be smoother than in the model-free case.

To validate our approach and evaluate the performance of the two controllers, we conducted several experiments, including a comparison of the two controllers, SS-actuators with different phases, and pressure tracking. The results of these experiments are presented in the following section.

V. Experiments and Discussion

Our experiment platform is shown in the Figure 7(A~C). Two different setups are used in the experiment, which is the setup using one pair of SS-actuators (Fig. 7B) and the setup using three pairs of SS-actuators (Fig. 7C). Both two setups apply the electrical diagram as shown in the Fig. 7A, where MOSSET functions as the PWM generator, and Arduino Mega2560 is used as controller for controlling the solenoid valves and motor. A 2L tank was selected as the target container, as it ensures that when using 2~6 SS-actuators, the pressure in the tank increases at a proper rate. In these experiments, the parameters of every SS-actuators are listed in Table. 1.

A. System Model Validation

Experiment of flow rate model. As per the analysis in the system modeling section, the flow rate model assumes identical inlet and outlet port pressures. To assess the accuracy of the flow rate model in this ideal condition and its performance in pressurizing conditions, we designed three experiments, as illustrated in Fig. 7(D~G).

To evaluate the flow rate model of a single SS-actuator and multiple SS-actuators, we set up experiments 1 and 2, respectively, with an angular velocity of 1 rad/s. The inlet port is connected to the atmosphere, and the outlet port is connected to the flowmeter and then to the atmosphere. The results of the one-SS-actuator experiment (Fig. 7D) indicate that the theoretical flow rate is in perfect agreement with the measured value. However, in the two-SS-actuators experiment (Fig. 7E), the results show a slight deviation from the theoretical prediction due to some air interference resulting from check-valve-controlled airflow. Specifically, we observe that air interference becomes worse when the motor operates at high speed or with multiple SS-actuators, which can be implicitly reflected by the average flow rate shown in Figure 9A. Although a higher speed or parallel connection of multiple SS actuators does not theoretically affect the flow rate, the check valves introduce some unpredictability to the actual flow rate.

To evaluate the flow rate model with a pressure difference between the inlet and outlet ports, we designed experiment 3. In this experiment, the outlet port was connected to a pressure sensor and a flowmeter, and then to the container, which causes a gradual increase in pressure during the pressurization process. The flow rate (Fig. 7F) fits perfectly with the trend of pressure increase before the pressure reaches 20 kPa. However, the flow rate prediction becomes increasingly inaccurate as the pressure increases. We also compared the pressure increase between one and two SS-actuators with the same configurations, as shown in Fig. 7G, from which we can observe that the pressure increase of one SS-actuator is smoother without the identical-pressure assumption. This means multiple SS-actuators have some airflow interference due to the solenoid valve switching.

Validation of average flow rate. We conducted experiments to validate the average flow rate model and investigate the pumping performance of the system under different motor speeds and SS-actuator quantities. In these experiments, we connected the flowmeter to the outlet or inlet port to collect positive or negative flow rates, respectively, without setting up a target container. We varied the motor speed and the number of SS-actuators, as shown in Figure 9A. In conclusion, this model accurately captures the flow rate feature of the SS pump. Besides, we found that the actual average flow rate is lower than the theoretical value, which attributes to the air interference. The air interference could be resulted from both the motion delay of the check valve and fluidic dynamics.

Moreover, according to the flow rate model, the average flow rate should be the same for both positive and negative pressure output. To verify this assumption, we conducted two experiments. In the first experiment, we fixed the motor speed at 2π rad/s and tested 1, 2, 4, and 6 SS-actuators. We observed a sequence of positive average flow rates: (2.72, 5.45, 10.71, 15.63) L/min, and negative flow rates: (-2.60, -5.22, -10.34, -14.29) L/min. In the second experiment, we used two SS actuators and tested the SS pump under the speed of 0.5π, π, 1.5π, 2π, and 2.5π rad/s. We observed a sequence of average flow rates: (1.39, 3.33, 4.47, 5.45, 6.06) L/min, with corresponding negative values of (-1.18, -3.24, -4.48, -5.22, -6.06) L/min. From these experiments, we conclude that positive and negative output have the same average flow rate when the system configuration is identical. However, the actual flow rate is slightly lower than the theoretical value due to the air interference.

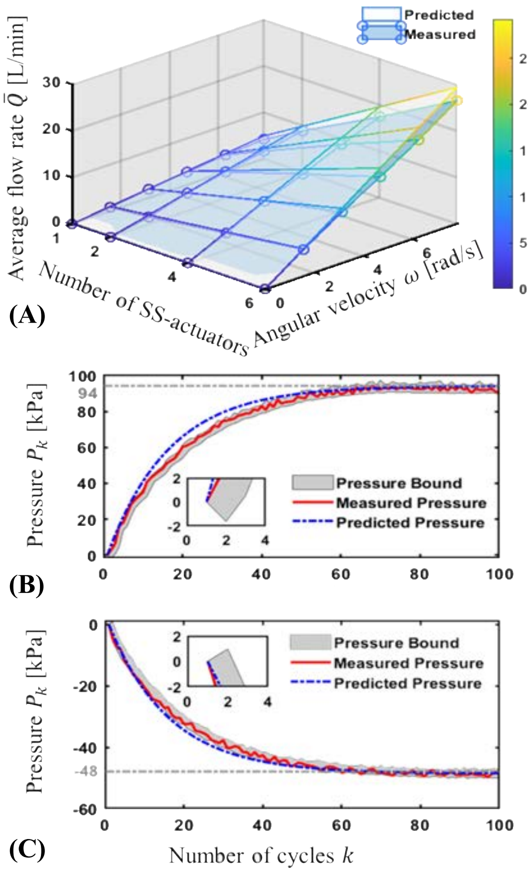

Figure 9. (A) Average flow rate with different number of SS-actuators and angular velocity. (B) and (C) are dynamic response of positive pressure and negative pressure. Keyframes are demonstrated by blue line, and grey area is the measured pressure bound for each cycle.

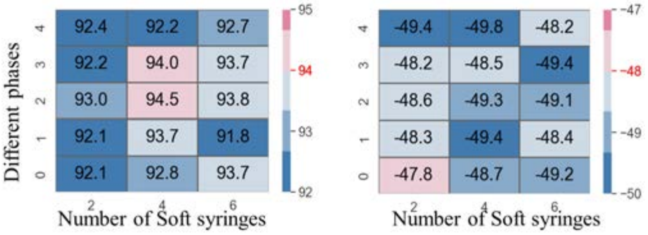

(A) (B)

Figure 10. (A) and (B) are the upper and lower pressure extremum respectively.

Validation of pressure extremum. In this experiment, we connected the output port of the system to a 2L tank and maintained the motor at a constant speed until the pressure oscillated periodically around a constant extreme value, which we defined as the pressure extremum. Three repeated experiments are conducted to obtain every average pressure extremum for each phase-actuators configuration. As shown in Figure 10(A, B), the red value is the nominal pressure extremum based on the soft syringe configuration in Table. I, and different phases configuration of the SS-actuators are applied. For example, for two SS-actuators, the phase difference is chosen as $(0, \frac{\pi}{4}, \frac{2\pi}{4}, \frac{3\pi}{4}, \frac{4\pi}{4})$, where the phase π is quartered. We can observe that different quantities of SS actuators and phases did not significantly affect the pressure extremum.

Keyframe of pressure dynamic response. The keyframe of the pressure dynamic response model is characterized by the periodic motion of the SS pump, which enables the description of the nonlinear properties of the pressure changes. At each cycle, the SS-actuator moves to a specific position, and we can derive the equilibrium relation (Eq. 10 and 11) to determine the pressure P_k at that position. However, predicting the pressure at other positions is challenging, as it depends on accurately detecting sensory feedback and predicting soft deformation.

To validate the keyframe model, we conducted two dynamic response experiments where the pump operated under inflation and extraction modes, respectively. The results are presented in Figure 9(B and C), where the x-axis denotes the number of cycles and the y-axis represents the output pressure. Although the pressure in the middle of the cycles is smaller than the theoretical value due to air interference, this did not impact the pressure extremum. Additionally, to analyze the pressure range in each cycle of dynamic response, we defined the bound pressure for every cycle in the gray area. The bound pressure at P_k is defined on t from $k-1$ to k.

As highlighted in Figure 9(B and C), there was an overshoot of the gray area at the keyframe P_1, which we assume is resulted from the inertia of the check valve. During the pressurizing process, the plunger moves backward after the start point P_0, and due to the hysteresis of the valve, the SS-actuator instantaneously generates negative pressure, which then gradually goes back to the atmosphere. Moreover, the keyframe curve P_k press close to one side of the pressure bound before the pressure reaches 70 kPa and -40 kPa, while increasingly conforming to the center of the gray area as the pressure increases. We assume this phenomenon reflects a decrease in energy efficiency: the closer the pressure reaches the saturation pressure, the more useless work the motor produces.

B. Pressure Control Performance

Performance of the model-free controller and model-based controller. Two different controllers are implemented in this experiment, which are model-free controllers and model-based controllers (Fig. 8(A, B)). The model-based controller differs from the model-free controller in that it employs a PID regulator and the forward model to achieve a smoother flow rate based on pressure error. The motor speed bound is set as $\pi\ rad/s$ without loss of generality.

In the experiment, as depicted in Figure 11(A, B), a desired pressure of 20 kPa was set, and a pair of SS-actuators was employed (Fig. 7B). Both controllers exhibited excellent control performance, but the model-based controller displayed smoother control performance in both rising and stable stages. However, to maintain the stability of the regulator's flow rate output, the angular velocity ω of the model-based controller demonstrated a singularity pattern, as analyzed in the system modeling section (Fig. 6B). This pattern resulted from $f(\theta + \theta_i) = 0$ (Eq. 6), for some θ of the paired SS-actuators and can be addressed by adjusting the phase between SS-actuators in multi-SS-actuators SS pump. In summary, the model-based pressure controller achieved a better control performance by mitigating pressure fluctuations during pressure regulation. This success further validates the accuracy of the model.

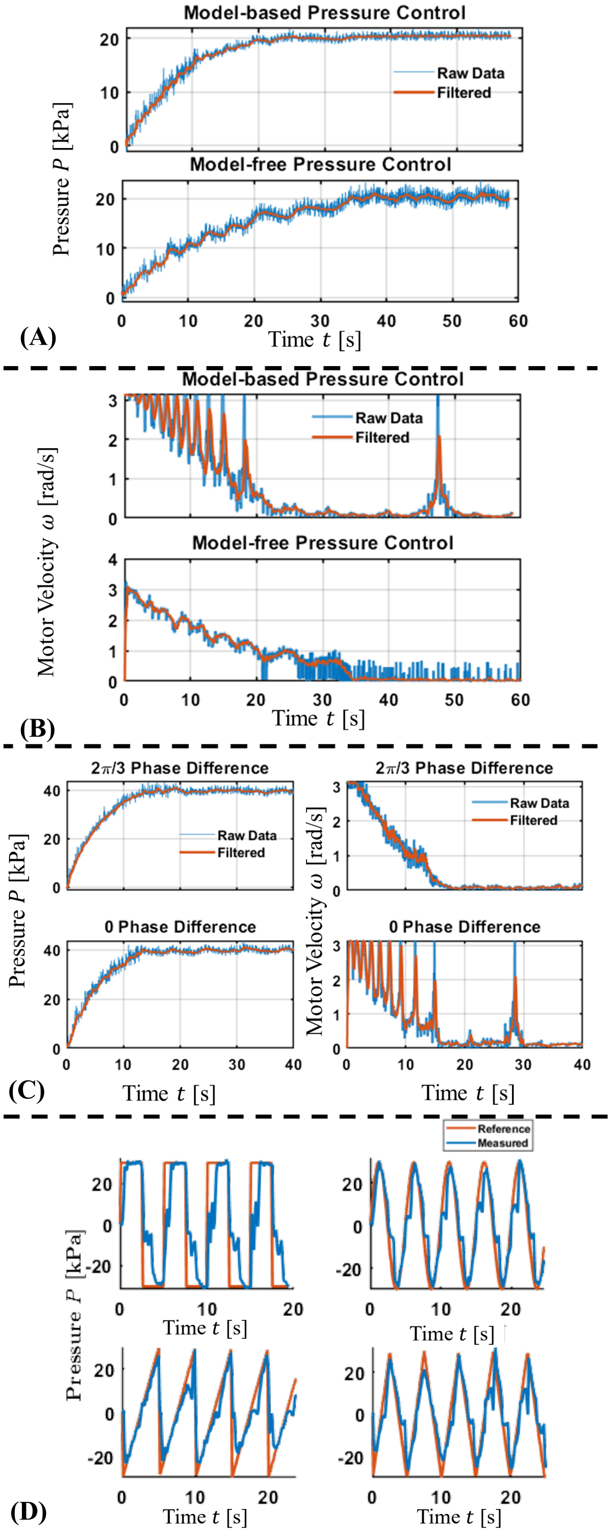

Figure 11. Control performance. (A) and (B) show the measured pressure and desired ω for model-based and model-free pressure control. (C) illustrates the performance of three pairs of bellows using two different phases. (D) Tracking performance of model-based pressure controller for different reference waveforms.

How the phase influences the control performance in multi-SS-actuators SS pump. The open-loop result is shown in the Fig. 6(D-F). The fluctuation and difference between the theoretical and measured flow rate could be from the local deformation of the PPF material and pneumatic system damping. As the 0-phase-difference configuration has singularity points, the motor velocity is supposed to reach the upper limit, 2 rad/s, and the flow rate approaches 0 near the singularity point, which fits the experiment results. On the other hand, 2π/3-phase-difference avoids the singularity and thus has a smoother flow rate and pressure change.

In closed-loop experiment, we employed a model-based controller for two SS pumps, each comprising three pairs of SS-actuators. The phase configuration of one SS pump was $(0, \pi, 0, \pi, 0, \pi)$, referred to as 0-phase-difference, while the other SS pump had a phase configuration of $(0, \pi, \frac{2\pi}{3}, \frac{5\pi}{3}, \frac{4\pi}{3}, \frac{7\pi}{3})$, referred to as 2π/3-phase-difference (Fig. 4G). It was observed that the singularity occurred when the $f(\theta + \theta_i)$ approached 0, and thus a more uniform phase distribution was considered to be smoother for the angular velocity. This observation was supported by the angular velocity figure and Fig. 11C. Additionally, 2π/3-phase-difference demonstrated a better control performance than 0-phase-difference with regard to tracking smoothness. We also observe that 0-phase-difference was less smooth than the model-based control of one pair of SS-actuators. This is because the increase in average flow rate made three pairs of SS-actuators more sensitive to the angular velocity than one pair of SS actuators, leading to less smooth pressure under the same angular velocity.

In summary, the results suggest that a uniform phase distribution leads to better pressure-tracking performance and a smoother change of angular velocity.

Experiments of pressure tracking. To evaluate the tracking performance of the model-based controller, we conducted experiments using four reference signals: square, sine, sawtooth, and triangular. We employed a 50 mL container for high-frequency tracking, essential for applications like robotic grasping, as most robotic suction cup or soft actuators typically have a volume not exceeding 50 mL. The maximum angular velocity set over 2.5π/s is acceptable.

Our results show that when the reference pressure suddenly steps between positive and negative pressure, as demonstrated by the square wave signal in Fig. 11D, the measured pressure tracks the reference with a delay of approximately one-quarter of one signal cycle. This delay can be attributed to the response time required by the continuous pumping controller to release the pressure to atmospheric pressure by changing the solenoid valve states and then gradually reaching the target by controlling the motor speed. As the frequency of the waveform increases, the delay becomes more pronounced, and there may not be enough time to approach the reference pressure before the signal steps in the opposite direction.

In contrast, the best pressure servo control performance is observed for the sine wave signal, as shown in Fig. 11D. Here, the measured and reference pressures overlap with almost no delays. The gradually changing reference signal gives the continuous pumping controller sufficient time to make adjustments, effectively tracking the signal waveform. The sawtooth and triangular signal waves are also well followed, as demonstrated in Fig. 11D.

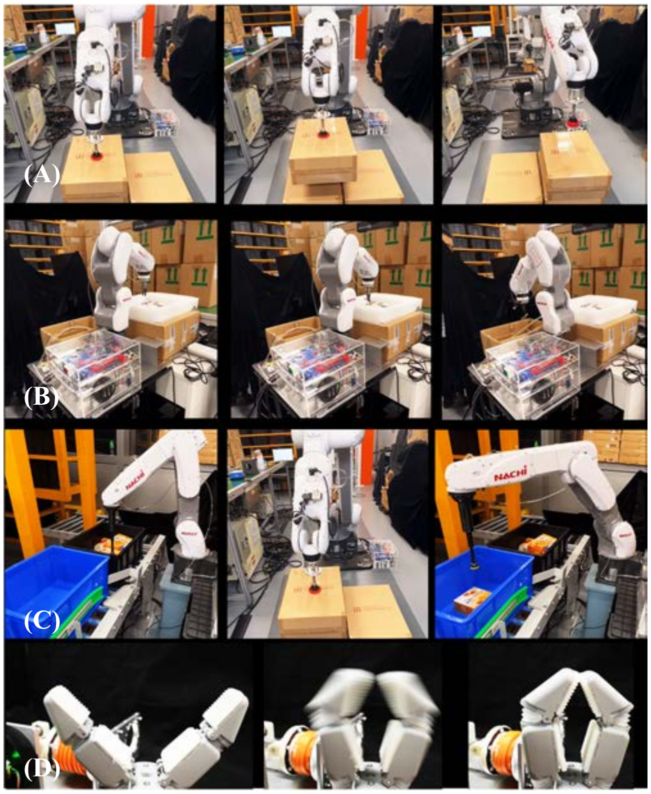

Figure 12. SS pump applications. (A) Suction application of industrial robot arm in palletizer. (B) Pneumatic two finger gripper in industrial picking. (C) Daily objects picking using suction cup. (D) Robotic hand operating at 6.5 Hz.

In summary, the SS pump demonstrates excellent pressure servo control performance, making it a versatile choice for various applications, where it can serve as a reliable source of programmed pressure.

C. Robotic applications

We applied the prototype SS pump to various robotics end-effector applications to validate its effectiveness. The study includes investigating objects picking with various sizes and weights, ranging from large logistics boxes to small metal components weighing between 50g to 400g, through various robotic end-effectors, as demonstrated in Figure 12(A~C). The SS pump actuation of continuous pumping and efficient pressure modulation ensures the high success of those pneumatic end-effectors' picking. Besides, a soft-rigid hybrid gripper pumping control under high frequency is demonstrated in Fig. 12D through direct pumping mode.

D. Noise Level, Pressure Range Testing, and Bandwidth

In addition, we conducted a comparative study on noise levels between the SS pump and four off-the-shelf pumps, as well as an experiment to assess the pressure range (Fig. 1E). The results of the noise experiment show that the average noise level of the off-the-shelf pumps is approximately 84 dB, while the mini-diaphragm pump (Rochu, ACU2-B) has an average noise level of 63 dB. The SS pump, in contrast, has an average noise level of 55.6 dB, validating its low noise superiority over traditional pumps. The safe pressure range reaches -0.082Mpa~0.153Mpa, which is associated with the material used for the soft syringe prototype. Within the safe pressure range, the soft syringe prototype successfully achieved 1000 times the full actuation durability test. Further enhancement of the fabrication material provides the potential to increase the pressure range.

Bandwidth refers to the range of frequencies over which the pump can operate effectively, thus, friction force and fluidic interference affect the bandwidth. The traditional rigid syringe, due to its high damping, experiences significant friction at elevated operating frequencies. When powered by the same motor, soft syringes achieve the motor's maximum frequency of 6.5Hz, whereas the rigid syringe reaches only 1.5Hz. This difference in bandwidth is expected to widen with an increase in motor speed. Fluidic interference is indicated by the growing discrepancy between the predicted and actual flow rates, as depicted in Fig. 9A. It is reasonable that there's a point where the flow rate decreases to the -3dB level when the frequencies increase.

VI. Conclusion and Future Work

We have proposed a novel soft syringe and presented the SS pump based on it that offers quiet, flexible pressure modulation and two-mode pneumatic pumping. The soft syringe features low friction, high frequency, low noise, and a sufficient pressure range with repeatable structural deformation, thus providing a viable solution to the pumping challenge. The modular and scalable two-mode pumping mechanism relies on multiple check valves with four solenoid valves, enabling the pump to provide direct pumping and continuous pumping. We have described the design, fabrication, modeling, and model-based pressure control of the SS pump and introduced a keyframe model to handle the nonlinearity of pressure dynamic response. Our work represents an important step towards the development of more efficient, flexible, and controllable pneumatic systems, which provides promising applications in the field of pneumatic robot actuation and control.

In future work, our primary objective will be to enhance the ease of mounting the Soft-Syringe (SS) pump by reducing the size of the SS actuator. This step is intended to facilitate the direct integration of the SS pump onto robotic arms, eliminating the requirement for a tethered setup and enabling seamless connectivity to end-effectors. Furthermore, we acknowledge the significance of addressing the dynamic behavior of the proposed pump system, encompassing both the dynamic behavior of the soft syringe and the controlled fluid. Therefore, exploring the dynamic behavior and investigating the effects of temperature will be of substantial importance.

Appendix

Nomenclature

a	Attained coefficient
θ	Actual motor rotation angle
θ_i	The phase of the i-th soft syringe
$\dot{\theta}$	Actual motor speed
q_i	Distance between the shaft to the i-th soft syringe
$\dot{q}_i$	The compressing velocity of the i-th soft syringe
ω	Desired motor rotation speed
V_i	The volume of the i-th soft syringe
$\dot{V}_i$	The volume change of the i-th soft syringe
Q_i	Flow rate of the i-th soft syringe
Q_r	The referenced flow rate
$\bar{Q}$	The average flow rate of the SS pump
T	Period of the motor
P_a	The pressure of atmosphere
ΔV	The changeable volume of the SS-actuator

REFERENCES

[1] G.-Z. Yang *et al.*, "The grand challenges of Science Robotics," *Sci. Robot.*, vol. 3, no. 14, p. eaar7650, Jan. 2018.

[2] C. Laschi, B. Mazzolai, and M. Cianchetti, "Soft robotics: Technologies and systems pushing the boundaries of robot abilities," *Sci. Robot.*, vol. 1, no. 1, p. eaah3690, Dec. 2016.

[3] M. R. Cutkosky, "On grasp choice, grasp models, and the design of hands for manufacturing tasks," *IEEE Trans. Robot. Autom.*, vol. 5, no. 3, pp. 269–279, Jun. 1989.

[4] A. Bicchi, "Hands for dexterous manipulation and robust grasping: a difficult road toward simplicity," *IEEE Trans. Robot. Autom.*, vol. 16, no. 6, pp. 652–662, Dec. 2000.

[5] J. Wallén, *The History of the Industrial Robot*. Linköping University Electronic Press, 2008. Accessed: Mar. 16, 2023.

[6] I. J. Karassik, Ed., *Pump handbook*, 4th ed. New York: McGraw-Hill, 2008.

[7] M. Volk, *Pump Characteristics and Applications, Third Edition*. CRC Press, 2013.

[8] R. S. Baker and M. J. Tessier, "Handbook of electromagnetic pump technology," Jan. 1987, Accessed: Mar. 16, 2023.

[9] D. Bach, F. Schmich, T. Masselter, and T. Speck, "A review of selected pumping systems in nature and engineering—potential biomimetic concepts for improving displacement pumps and pulsation damping," *Bioinspir. Biomim.*, vol. 10, no. 5, p. 051001, 2015.

[10] C. Liu, Y. Wang, L. Ren, and L. Ren, "A Review of Biological Fluid Power Systems and Their Potential Bionic Applications," *J. Bionic Eng.*, vol. 16, no. 3, pp. 367–399, May 2019.

[11] J. Zhou *et al.*, "A soft-robotic approach to anthropomorphic robotic hand dexterity," *Ieee Access*, vol. 7, pp. 101483–101495, 2019.

[12] T. Ren, Y. Li, M. Xu, Y. Li, C. Xiong, and Y. Chen, "A Novel Tendon-Driven Soft Actuator with Self-Pumping Property," *Soft Robot.*, vol. 7, no. 2, pp. 130–139, Apr. 2020.

[13] W. Tang *et al.*, "Customizing a self-healing soft pump for robot," *Nat. Commun.*, vol. 12, no. 1, p. 2247, Apr. 2021.

[14] C. Cao, X. Gao, and A. T. Conn, "A Magnetically Coupled Dielectric Elastomer Pump for Soft Robotics," *Adv. Mater. Technol.*, vol. 4, no. 8, p. 1900128, 2019.

[15] G. Mao *et al.*, "Design and characterization of a soft dielectric elastomer peristaltic pump driven by electromechanical load," *IEEEASME Trans. Mechatron.*, vol. 23, no. 5, pp. 2132–2143, 2018.

[16] R. S. Diteesawat, T. Helps, M. Taghavi, and J. Rossiter, "Electro-pneumatic pumps for soft robotics," *Sci. Robot.*, vol. 6, no. 51, p. eabc3721, 2021.

[17] M. Li, A. Pal, A. Aghakhani, A. Pena-Francesch, and M. Sitti, “Soft actuators for real-world applications,” *Nat. Rev. Mater.*, vol. 7, no. 3, Art. no. 3, Mar. 2022.

[18] J. Zhou, Y. Chen, X. Chen, Z. Wang, Y. Li, and Y. Liu, “A proprioceptive bellows (PB) actuator with position feedback and force estimation,” *IEEE Robot. Autom. Lett.*, vol. 5, no. 2, pp. 1867–1874, 2020.

[19] H. Liu, C. Wu, S. Lin, Y. Li, and Y. Chen, “Double-Acting Soft Actuator for Soft Robotic Hand: A Bellow Pumping and Contraction Approach,” *Biomimetics*, vol. 7, no. 4, Art. no. 4, Dec. 2022.

[20] K. Lee, P.-G. Jung, and Y. Cha, “Origami Pump Based on Planetary Gear System for Pneumatic Pressure,” *IEEEASME Trans. Mechatron.*, vol. 28, no. 3, pp. 1436–1445, Jun. 2023.

[21] Y. Yang, Y. Xie, J. Liu, P. Jiang, and Y. Chen, “Self-Pumping Actuation Module and its Application in Untethered Soft Robots,” *J. Intell. Robot. Syst.*, vol. 108, no. 2, p. 16, Jun. 2023.

[22] J.-G. Lee and H. Rodrigue, “Origami-Based Vacuum Pneumatic Artificial Muscles with Large Contraction Ratios,” *Soft Robot.*, vol. 6, no. 1, pp. 109–117, Feb. 2019.

[23] D. C. F. Li, Z. Wang, J. Zhou, and Y.-H. Liu, “Honeycomb Jamming: An Enabling Technology of Variable Stiffness Reconfiguration,” *Soft Robot.*, vol. 8, no. 6, pp. 720–734, Dec. 2021.

[24] Y. Li *et al.*, “Untethered Multimode Fluidic Actuation: A New Approach to Soft and Compliant Robotics,” *Soft Robot.*, vol. 8, no. 1, pp. 71–84, Feb. 2021.

[25] J. Zhou, H. Cao, W. Chen, S. S. Cheng, and Y.-H. Liu, “Bioinspired Soft Wrist Based on Multicable Jamming With Hybrid Motion and Stiffness Control for Dexterous Manipulation,” *IEEEASME Trans. Mechatron.*, pp. 1–12, 2022.

[26] H. Cao, W. Chen, Y. Lu, J. Huang, J. Zhou, and Y. Liu, “An End-to-End Proprioception Framework for Soft Continuum Robot,” in *2022 IEEE International Conference on Robotics and Biomimetics (ROBIO)*, Dec. 2022, pp. 141–147.

[27] Y. Li, R. Tao, Y. Li, Y. Yang, J. Zhou, and Y. Chen, “A Highly Adaptive Robotic Gripper Palm with Tactile Sensing,” in *2022 IEEE International Conference on Real-time Computing and Robotics (RCAR)*, Jul. 2022, pp. 130–135.

[28] J. Zhou, Y. Li, Y. Yang, H. Cao, J. Huang, and Y. Liu, “A 22-DOFs Bio-inspired Soft Hand Achieving 6 Kinds of In-hand Manipulation,” in *2021 IEEE International Conference on Real-time Computing and Robotics (RCAR)*, Jul. 2021, pp. 20–26.

[29] J. Zhou, S. Chen, and Z. Wang, “A Soft-Robotic Gripper With Enhanced Object Adaptation and Grasping Reliability,” *IEEE Robot. Autom. Lett.*, vol. 2, no. 4, pp. 2287–2293, Oct. 2017.

[30] J. Huang *et al.*, “Modular origami soft robot with the perception of interaction force and body configuration,” *Adv. Intell. Syst.*, vol. 4, no. 9, p. 2200081, 2022.

[31] H. Cao *et al.*, “Two-Stage Grasping: A New Bin Picking Framework for Small Objects.” arXiv, Mar. 07, 2023.

[32] A. Zaghloul and G. M. Bone, “3D Shrinking for Rapid Fabrication of Origami-Inspired Semi-Soft Pneumatic Actuators,” *IEEE Access*, vol. 8, pp. 191330–191340, 2020.

[33] J.-G. Lee and H. Rodrigue, “Efficiency of Origami-Based Vacuum Pneumatic Artificial Muscle for Off-Grid Operation,” *Int. J. Precis. Eng. Manuf.-Green Technol.*, vol. 6, no. 4, pp. 789–797, Aug. 2019.

[34] H. Jiang *et al.*, “Hierarchical control of soft manipulators towards unstructured interactions,” *Int. J. Robot. Res.*, vol. 40, no. 1, pp. 411–434, Jan. 2021.

[35] L. Wang and Z. Wang, “Mechanoreception for Soft Robots via Intuitive Body Cues,” *Soft Robot.*, vol. 7, no. 2, pp. 198–217, Apr. 2020.

[36] M. Wehner *et al.*, “Pneumatic Energy Sources for Autonomous and Wearable Soft Robotics,” *Soft Robot.*, vol. 1, no. 4, pp. 263–274, Dec. 2014.

[37] M. S. Xavier, A. J. Fleming, and Y. K. Yong, “Design and Control of Pneumatic Systems for Soft Robotics: A Simulation Approach,” *IEEE Robot. Autom. Lett.*, vol. 6, no. 3, pp. 5800–5807, Jul. 2021.

[38] Y. Zhao, Y. Li, L. Sentis, U. Topcu, and J. Liu, “Reactive task and motion planning for robust whole-body dynamic locomotion in constrained environments,” *Int. J. Robot. Res.*, vol. 41, no. 8, pp. 812–847, Jul. 2022.

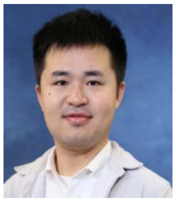

Jianshu Zhou (Member, IEEE) received the Ph.D. degree from the Department of Mechanical Engineering, The University of Hong Kong, 2020. He serves as a research assistant professor at The Chinese University of Hong Kong. His research includes robotics, grasping and manipulation, robotic hands, embodied intelligence, and proprioceptive system.

Junda Huang received the B.Eng. degrees from the University of Science and Technology of China (USTC) in 2020. Currently, he is pursing the Ph.D. degree at the CUHK. His research interest includes robotics, robotic grasping and manipulation, and robot control.

Xin Ma received the B.Eng. and Ph.D. degrees in mechanical and electronic engineering from Dalian University of Technology, Dalian, China, in 2011 and 2017, respectively. From 2017 to 2019 he was at The Chinese University of Hong Kong, as Research Postdoctoral Fellow. From 2019 to 2021 he was at Purdue University, as Postdoctoral Fellow. He is currently a Research Assistant Professor at The Chinese University of Hong Kong. He is doing robotics, medical robots, and flexible robots.

Andy received the B.E. degree from SCUT in 2018 and Msc from CUHK in 2020. He is doing motion planning on auto-store, DB Schenker warehouse, and WSD water testing for commercialization and his PhD degree under Prof. Liu Yunhui.

Kazuhiro Kosuge (Fellow, IEEE) received the B.S., M.S, and Ph.D. degrees in control engineering from the Tokyo Institute of Technology, Tokyo, Japan, in 1978, 1980, and 1988 respectively. He is currently the chair Professor with the Department of Electrical and Electronic Engineering, the University of Hong Kong. Prof. Kosuge was the recipient of the JSME Awards for the best papers from the Japan Society of Mechanical Engineers in 2002 and 2005, the RSJ Award for the best papers from the Robotics Society of Japan in 2005. He was the President of the IEEE Robotics and Automation Society for 2010-2011 and the IEEE Division X Director for 2015-2016. He is a member of the IEEE-Eta Kappa Nuand the IEEE Vice President for Technical Activities for 2019.

Yun-Hui Liu (Fellow, IEEE) received the B.Eng. degree from the Beijing Institute of Technology, the M.Eng. degree from Osaka University, and the Ph.D. degree from The University of Tokyo in 1992. After working at the Electrotechnical Laboratory, Japan, as a Research Scientist, he joined The Chinese University of Hong Kong (CUHK) in 1995, where he is currently a Choh-Ming Li Professor of mechanical and automation engineering and the Director of the CUHK T Stone Robotics Institute. He is also an Adjunct Professor at the State Key Laboratory Robotics Technology and System, Harbin Institute of Technology, China. He has published more than 300 articles in refereed journals and refereed conference proceedings and was listed in the Highly Cited Authors (Engineering) by Thomson Reuters in 2013. His research interests include visual servoing, medical robotics, multi-fingered grasping, mobile robots, and machine intelligence. He has received numerous research awards from international journals and international conferences in robotics and automation and government agencies. He was the Editor-in-Chief of *Robotics and Biomimetics* and served as an Associate Editor for the IEEE TRANSACTIONS ON ROBOTICS AND AUTOMATION and the General Chair for the 2006 IEEE/RSJ International Conference on Intelligent Robots and Systems.